Electronic Supplementary Material

Femtosecond Laser Induced Spin Dynamics in Single Layer Graphene/CoFeB Thin Films

*Surya Narayan Panda, Sudip Majumder, Samiran Choudhury, Arpan Bhattacharya, Sumona Sinha, Anjan Barman**

S-I. Micro-Raman Spectroscopy Analysis:

The micro-Raman scattering experiment (wavelength = 532 nm, microscope objective: 100X, grating: 600 g/mm, N.A. = 0.9 and spot diameter ≈ 0.7 μm) was carried out using a micro-Raman setup comprising a spectrometer (model Lab Ram HR Evolution, Horiba France SAS) and a thermoelectrically-cooled charge-coupled device (CCD) detector with 1024×256 pixel resolution to characterize the graphene layer, and underpin the effects of CoFeB deposition on graphene. The main features in the Raman spectra of carbon-based materials are the G and D peaks observed at 1586.8 and 1341 cm^{-1}, respectively. The G peak corresponds to the optical E_{2g} phonons at the Brillouin zone center, whereas the D peak is caused by transverse optical phonons near the K point of hexagonal ring and requires structural defects for its activation via an intervalley double-resonance.[1] It is present in defective carbon materials and its intensity (I_D) is proportional to the defect concentration in graphene.[1, 2] Higher I_D signifies that the sp^2 bonds in graphene are broken, which, in turn, means that there are more sp^3 bonds and transformation from sp^2 dominance to sp^3 dominance in the material. Its overtone, the 2D peak, appears at around 2678.9 cm^{-1}. There is also a peak at around 1623 cm^{-1}, called D′-peak, which occurs via an intravalley double-resonance process in the presence of defects. A combination mode (D + D′) appears at around 2939 cm^{-1} which also requires defects for its activation. We notice that I_D decreases by a factor of 14 when

CoFeB thickness increases from 1.5 to 6.0 nm (as shown in Fig. S1(a) and Fig. S1(b)), which signifies decrease in defect concentration in the graphene with an increase in CoFeB layer thickness. Intensities of D-peak and G-peak (I_G) decrease with an increase in CoFeB layer thickness despite maintaining identical external conditions (as shown in Fig. S1(b)). However, rate of decrease of I_G is much smaller in comparison to that of I_D which results in a decrease in spectral weight ratio (I_D/I_G ratio) with an increase in CoFeB layer thickness (as shown in Fig. S1(c)). Furthermore, perfect Lorentzian shaped 2D peak (which is shown in inset of Fig. S1(b)) proves single layer nature of graphene. The average crystallite size (L_a), which is a measure of the average distance between two adjacent defects, can be calculated using the relation:[5]

$$L_a = (2.4 \times 10^{-10})\, \lambda^4 \,(I_D/I_G)^{-1} \qquad \text{(S1)}$$

Here I_G is the G-peak intensity and λ is the excitation wavelength (532 nm). Fig. S1(d) shows there is an increase of L_a with the CoFeB thickness which indicate a decrease in defect density at higher CoFeB thicknesses.[5, 6] This decrease in defect density with an increase in CoFeB thickness also indicates a decrease in the defect-induced extrinsic effects with CoFeB thickness.

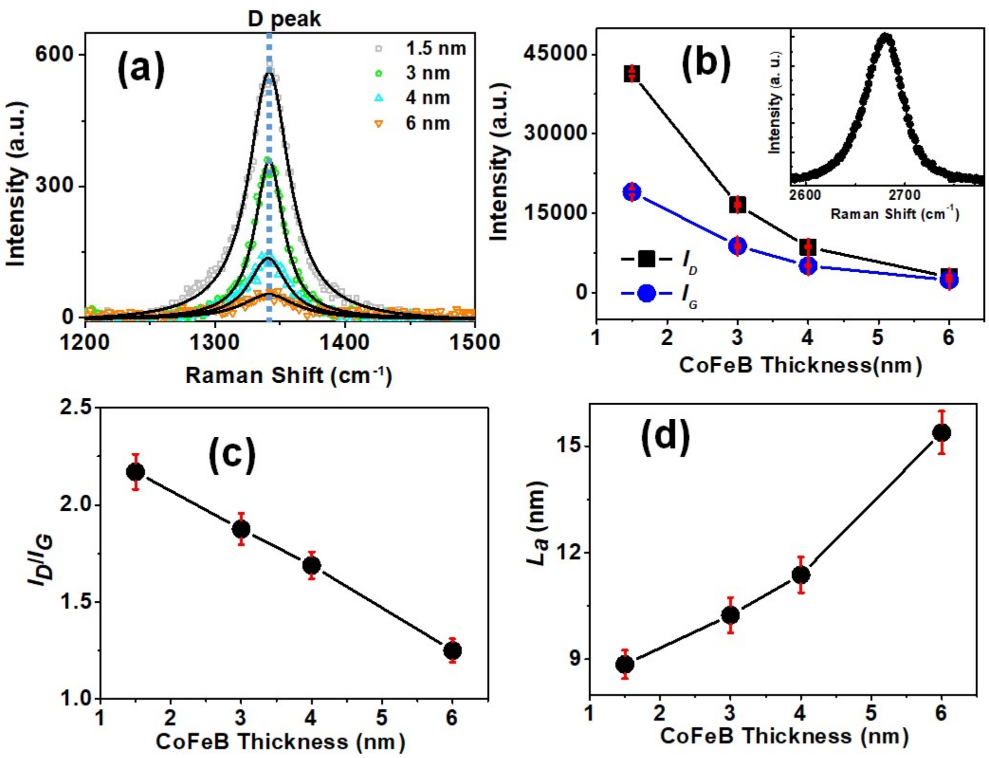

Fig. S1. (a) Variation of D peak of Raman spectra with CoFeB thickness. Scattered symbols are the experimental data points and solid lines are Lorentzian fits. (b) Variation of D peak intensity (I_D) and G peak intensity (I_G) with CoFeB thickness. Inset shows perfect Lorentzian shaped 2D peak for Raman spectra of SLG. (c) Variation of I_D/I_G ratio with CoFeB thickness. (d) Variation of average crystallite size (L_a) with CoFeB thickness.

S-II. Interfacial Roughness Obtained from AFM and XRR Measurements

AFM Measurement: We have also measured the surface topography of Sub/SLG/$Co_{20}Fe_{60}B_{20}$ (*d*)/SiO_2 (2 nm) thin films using atomic force microscopy (AFM) in dynamic tapping mode by taking scans over 2 μm × 2 μm area. Due to the small thicknesses of our thin films, the interfacial roughness must exhibit its imprint on the topographical roughness. We have analyzed the AFM images using WSxM software.[7] Also, variation in surface roughness very small when measured at different regions of the same sample. AFM images obtained for different CoFeB thicknesses in the presence of SLG is shown in Fig. S2(a). Average topographical roughness values obtained from AFM measurement is plotted in Fig. S2(b). Average topographical roughness obtained from AFM is found to monotonically decrease with CoFeB thickness in the presence of SLG.

X-ray Reflectivity Measurement: Grazing-incidence X-ray reflectivity (XRR) is a powerful technique for non-destructive probing of the structure of surface and interfaces. X-ray specular reflectivity measurements provide information about the interfacial roughness, thickness, and average electron density of different sub-layers of a thin film. We measured the XRR-spectra of Sub/SLG/$Co_{20}Fe_{60}B_{20}$ (*d*)/SiO_2 (2 nm) thin films using 8 KeV X-ray source and analyzed the spectra using Parratt's formalism. Average surface roughness obtained from the fit is plotted in Fig. S2(b) which shows that for lower CoFeB thickness (< 4 nm) roughness is higher as opposed to higher CoFeB thickness (≥ 4 nm). However, the roughness values obtained from AFM measurements are slightly lower than those obtained from XRR measurements. Electron densities of CoFeB, SLG and SiO_2 are found to be 15.0×10^{-5}, 1.5×10^{-5} and, 2.0×10^{-5} Å^{-2}, respectively, independent of CoFeB layer thickness (Shown in Fig. S2(c)).

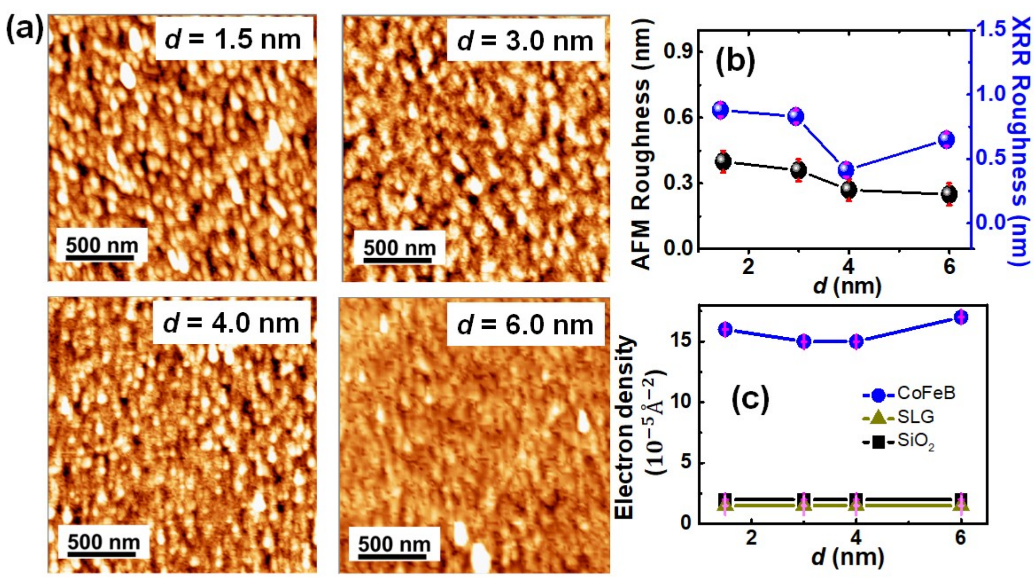

Fig. S2. (a) AFM images for Sub/SLG/CoFeB(*d*)/SiO_2(2 nm) samples. (b) Comparison between average roughness vs. CoFeB thickness obtained from AFM and XRR measurements. (c) Variation of electron density of SLG, CoFeB and SiO_2 with CoFeB thickness measured using XRR measurement.

S-III. Ultrafast Demagnetization and Its Correlation with Gilbert Damping:

Intercorrelation between ultrafast demagnetization time (τ_m) and Gilbert damping parameter(α) is of significant interest in recent times, as both share similar physical processes. Initially, based on the local phonon-mediated Elliott-Yafet scattering mechanism an inverse relationship between τ_m and α was predicted by B. Koopmans. *et al.*[8] Later experimental studies on rare-earth-doped Permolloy[9] and TbFeCo[10] found few drawbacks in this prediction due to the presence 4f bands which results in opening of an extra dissipation channel due to repopulation of states and distortion of the lattice. Following this, Fahnle et al.[11] showed that α can either be proportional or inversely proportional to τ_m depending upon the major microscopic contribution to it. When the damping is dominated by intra-band conductivity-like contribution there is a linear relationship between τ_m and α, whereas the inter-band resistivity-like contribution leads to an inverse relation. However, this model is proved to be effective only for the simple ferromagnetic system like Fe, Ni or Co without considering the effect of spin current transport, interfacial band hybridization and spin-orbit coupling. Recently an effective method is proposed and experimentally validated for bilayers and more complicated systems for unifying the τ_m and α to distinguish the dominant mechanism for ultrafast demagnetization.[12,13] According to this, a proportional relation between the τ_m and α indicates that the local spin-flip scattering mechanism dominates the ultrafast demagnetization process. However, an inverse dependence of τ_m on α indicates that the nonlocal spin transport mechanism dominates the ultrafast demagnetization process. In the presence of effects like spin pumping in a system, interfacial spin accumulation and its dissipation by spin current transport can open an additional channel to decrease the τ_m and enhance the α.

S-IV. Transient Reflectivity and Kerr Rotation:

We have examined whether the Kerr rotation corresponding to the demagnetization curves originates primarily from magnetic effects or any optical effects caused by the femtosecond laser irradiation make significant contribution in it. Here, we have presented the temporal variation of the normalized reflectivity and Kerr rotation in Fig. S3(a) and Fig. S3(b), respectively, for Sub/SLG/ CoFeB (3 nm)/ SiO_2 (2 nm). Fig. S3(c) shows the relative variation of the time-resolved reflectivity and Kerr rotation with CoFeB thickness which clearly shows that the reflectivity signal is much smaller than the Kerr rotation, implying negligible non-magnetic contributions in the Kerr rotation data in general.

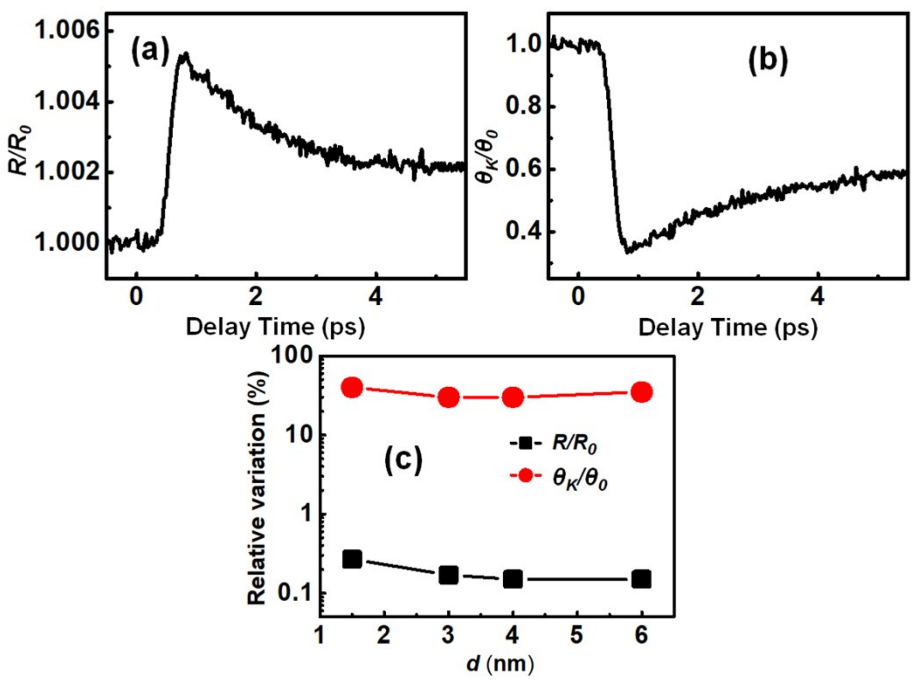

Fig. S3. (a) Transient reflectivity for Sub/SLG/CoFeB(3 nm)/SiO_2(2 nm) at pump fluence of 5 mJ/cm^2 normalized *w.r.t.* the corresponding negative delay value. (b) Transient Kerr rotation for Sub/SLG/CoFeB (3 nm)/SiO_2(2 nm) normalized *w.r.t.* the corresponding negative delay value. (c)

Relative variation of the peak values of transient Kerr rotation and reflectivity for varying CoFeB thickness.

S-V. Bias Field Dependent Precession Frequency and Damping

The variation of precessional dynamics with bias magnetic field (*H*) at a pump fluence of 5 mJ/cm^2 for SLG/CoFeB(3 nm)/SiO_2(2 nm) is shown in Fig. S4(a). The precessional oscillation is fitted with damped sinusoidal function of eq 4 of the article for extracting the relaxation time (τ) and precessional frequency(*f*). The effective saturation magnetization (M_{eff}) of the samples is obtained by fitting *f* vs. *H* data with the Kittel formula (eq 5) (see Fig. S4(b)). We have extracted the interfacial magnetic anisotropy energy density (K_s) and saturation magnetization(M_S) which is an indicator of the strength of the interfacial spin-orbit coupling (ISOC) by fitting the CoFeB thickness(*d*)-dependent M_{eff}(see Fig. S4(c)) with the formula:[14]

$$4\pi M_{eff} = 4\pi M_S - \frac{2K_s}{M_s d} \qquad \text{(S2)}$$

From the fit, we have extracted the values of interfacial magnetic anisotropy energy density (K_s), which is an indicator of the strength of the interfacial spin-orbit coupling (ISOC), to be 0.655 ± 0.02 erg/cm^2 in presence and absence of the SLG underlayer. However, saturation magnetization (M_s) decreases from 1327 ± 46 emu/cc in absence of SLG to 1220 ± 34 emu/cc in presence of SLG underlayer. This decrease in M_s can be attributed to the charge transfer from CoFeB to SLG and induced hybridization between graphene π-band and d-band of Co/Fe. After finding τ and M_{eff} from the experiment, we have extracted the Gilbert damping (α) by using eq 6 of the article. Variation of α with the bias magnetic field is plotted in Fig. S4(d). The α reduces monotonically with the increase in bias magnetic field and saturates at higher fields. For extracting both intrinsic and extrinsic contributions it can be fitted with the equation below:[13]

$$\alpha = \alpha_0 + \alpha_{ext} = \alpha_0 + \alpha_1 e^{-H/H_0} \quad \text{(S3)}$$

Here α_0 and $\alpha_1 e^{-H/H_0}$ are intrinsic and extrinsic contribution to the damping. The literature shows that the Gilbert damping due to two-magnon scattering increases with applied magnetic field because of the increased degeneracy of spin waves. However, in our studied system we have observed nearly constant Gilbert damping at higher applied magnetic fields, indicating minor contributions from the two-magnon scattering and surface inhomogeneity to precessional oscillation. All the thickness dependent studies have been performed at a high bias magnetic field of 3.59 kOe to ensure negligible extrinsic contribution for all studied samples.

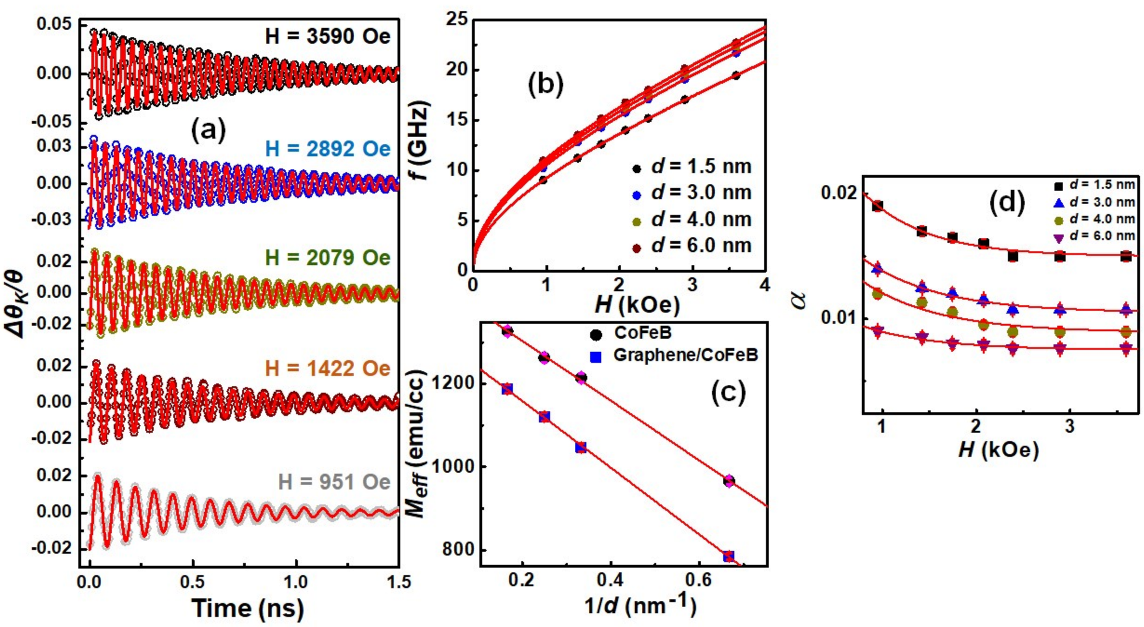

Fig. S4. (a) Bias magnetic field dependent time-resolved Kerr rotation data for Sub/SLG/CoFeB (3 nm)/SiO_2 (2 nm) showing precessional oscillations. Symbols are experimental data points and solid red lines are fit using eq 4 of the article. (b) Variation of *f* with *H* for Sub/SLG/CoFeB(*d*)/SiO_2(2 nm) samples. Symbols are experimental data points and solid red lines are fits using eq 5 of the article. (c) Variation of M_{eff} with 1/*d*. Symbols are experimental data points and solid red lines are fits using eq S2. (d) Variation of α with H. Symbols are experimental data points and solid red lines are fits using eq S3.

References:

[1] A.C. Ferrari, and D.M. Basko, *Nat. Nanotechnol.*, 2013, **8**, 235-246.

[2] P**.** Venezuela, M. Lazzeri, and F. Mauri, *Phys. Rev. B***,** 2011, **84**, 035433.

[3] A. C. Ferrari, *Solid State Commun.* 2007, **143**, 47.

[4] T. Mashoff, D. Convertino, V. Miseikis, C. Coletti, V. Piazza, V. Tozzini, F. Beltram, and S. Heun, *Appl. Phys. Lett.*, 2015, **106**, 083901.

[5] L. G. Cançado, K. Takai, T. Enoki, M. Endo, Y. A. Kim, H. Mizusaki, A. Jorio, L. N. Coelho, R. Magalhães-Paniago, and M.A. Pimenta, *Appl. Phys. Lett.*, 2006, **88**, 163106.

[6] A. K. Chaurasiya, A. Kumar, R. Gupta, S. Chaudhary, P. K. Muduli, and A. Barman, *Phys.Rev. B*, 2019, **99**, 035402.

[7] I. Horcas, R. Fernández, J. M. Gómez-Rodríguez, J. Colchero, J. Gómez-Herrero, and A. M. Baro, *Rev. Sci. Instrum*. 2007, **78**, 013705.

[8] B. Koopmans, J. J. M. Ruigrok, F. D. Longa, and W. J. M. de Jonge, *Phys. Rev. Lett.* 2005, **95**, 267207.

[9] J. Walowski, G. Müller, M. Djordjevic, M. Münzenberg, M. Kläui, C. A. F. Vaz, and J. A. C. Bland, *Phys. Rev. Lett.* 2008, **101**, 237401.

[10] Y. Ren, Y. L. Zuo, M. S. Si, Z. Z. Zhang, Q. Y. Jin, and S. M. Zhou, *IEEE Trans. Magn.* 2013, **49**, 3159-3162.

[11] M. Fähnle, J. Seib, and C. Illg, *Phys. Rev. B,* 2010**, 82**, 144405.

[12] W. Zhang, W. He, X. Q. Zhang, Z. H. Cheng, J. Teng, and M. Fähnle, *Phys. Rev. B,* 2017**, 96**, 220415.

[13] W. Zhang, Q. Liu, Z. Yuan, K. Xia, W. He, Q. F. Zhan, X. Q. Zhang, and Z. H. Cheng, *Phys. Rev. B,* 2019**, 100**, 104412.

[14] G. Wu, Y. Ren, X. He, Y. Zhang, H. Xue, Z. Ji, Q. Y. Jin, and Z. Zhang, *Phys. Rev. Appl.*, 2020, **13**, 024027.